

Evolution of a Single Impurity Across the Superfluid–Mott insulator Transition in the Bose–Hubbard Model

Chao Zhang^{1,*}

¹*Department of Physics, Anhui Normal University, Wuhu 241002, China*

We investigate how the coherence and spatial dressing of a single impurity evolve in the two-dimensional Bose–Hubbard model when the impurity couples attractively to the bath. Using large-scale, sign-problem-free quantum Monte Carlo simulations based on the worm algorithm, we track the impurity winding number, the bath superfluid density and compressibility, and impurity–bath density correlations. First, by fixing the bath interaction at $U_b/t = 13.3$ in the superfluid regime and tuning the attractive impurity–bath coupling from $U_{ib}/t = -1.0$ to -40.0 , we uncover an interaction-driven winding-collapse localization: the impurity evolves from a mobile light polaron with finite winding to a heavy polaron and, finally, to a bound cluster with vanishing winding, while the bath remains globally superfluid. Second, we analyze impurity in Mott-insulating baths for both attractive and repulsive impurity–bath couplings, contrasting the resulting deformation clouds and localization patterns. Third, for a moderate attractive impurity–bath coupling $U_{ib}/t = -8.0$, we tune the bath interaction U_b/t across the superfluid–Mott-insulator transition. The impurity evolves from a mobile light polaron with an extended deformation cloud in the superfluid to a nearly free defect propagating in an incompressible Mott-insulating background; for this moderate attraction it does not develop into a fully localized defect with a strictly local dressing cloud, even deep in the Mott insulator phase. This evolution constitutes a compressibility-controlled localization crossover of coherent impurity motion. Finally, together with our companion Letter [*The Fate of a Single Impurity in the Bose–Hubbard Model*], which focused on repulsive impurity–bath couplings, these results provide a unified microscopic picture of impurity localization in the Bose–Hubbard model, connecting interaction-driven and compressibility-controlled mechanisms across both attractive and repulsive regimes.

I. INTRODUCTION

The behavior of a single impurity immersed in a quantum many-body medium provides a sensitive probe of correlations, coherence, and emergent quasiparticles. In weakly interacting Bose gases, such an impurity forms a Bose polaron: a dressed quasiparticle characterized by a finite quasiparticle residue, renormalized effective mass, and an extended bath density cloud [1–9]. In the continuum, Bose polarons have been observed and characterized with high precision using radio-frequency and Ramsey spectroscopy in ultracold atomic mixtures [10–12], and their properties across weak to strong coupling have been mapped out both experimentally and theoretically [1]. These studies have established the continuum Bose polaron as a paradigmatic example of an impurity problem in a quantum fluid.

Beyond continuum Bose gases, optical lattices offer a complementary platform where the bath is naturally described by the Bose–Hubbard model (BHM) [13–16], providing a controlled setting to study a single mobile impurity in a strongly correlated lattice Bose fluid. By tuning the ratio between on-site repulsion and tunneling, the BHM realizes a quantum phase transition from a compressible superfluid (SF) to an incompressible Mott insulator (MI), as first observed in pioneering cold-atom experiments [17]. With the advent of quantum gas microscopy, site-resolved imaging and control of individual atoms in optical lattices has become possible [18, 19], including the preparation and tracking of single impurity or spin excitation in Bose–Hubbard chains and 2D lattices [20]. This opens the door to directly visualizing how an impurity

propagates, dresses, and eventually localizes as the background evolves from SF to MI.

Theoretical work on lattice Bose polarons and impurities in the BHM has addressed a number of important limits [21–26]. Variational approaches have explored mobile impurities near the SF–MI transition [24], and recent large-scale quantum Monte Carlo (QMC) simulations have analyzed the “Bose–Hubbard polaron” from weak to strong impurity–bath coupling in two dimensions [27]. In particular, Ref. [27] used worm-algorithm QMC in the grand-canonical ensemble to show that, at weak coupling, polaron spectral properties such as the effective mass can serve as a sensitive probe of the MI–SF transition, while at strong coupling the impurity binds an extra particle or hole in the MI, leading to novel bound states beyond the simple polaron picture. Nevertheless, most lattice studies to date have focused primarily on *impurity* spectral observables—energy shifts, effective masses, and spectral functions—and typically emphasized either the SF side or the MI side separately, with the bath entering only through averaged properties. What is still lacking is a unified, real-space characterization that follows *both* the impurity’s coherent mobility and the associated impurity-centered bath density deformations across the superfluid–Mott insulator transition.

In a recent companion Letter [28], we addressed the fate of a single mobile impurity in the two-dimensional Bose–Hubbard model at unit filling by mapping out its regimes in the plane of bath interaction U_b/t and local impurity–bath coupling U_{ib}/t [28]. Using sign-problem-free multi-species worm-algorithm quantum Monte Carlo (QMC) simulations in the grand-canonical ensemble [29? , 30], we demonstrated that impurity localization in this setting can be realized via two distinct yet unified routes. (i) Along lines of varying impurity–bath coupling U_{ib}/t at fixed bath parameters in a SF bath, localization is driven by an *interaction-driven winding-collapse*

* chaozhang@ahnu.edu.cn

crossover: a weakly coupled impurity forms a mobile light polaron with finite winding and an extended dressing cloud, whereas increasing $|U_{\text{ib}}|/t$ leads to the collapse of impurity winding while the bath remains globally superfluid, signaling a heavy self-trapped state and, for repulsive $U_{\text{ib}}/t > 0$, finally a depletion saturated-bubble state. (ii) Along lines of varying bath interaction U_b/t , where the bath evolves from a SF to a MI state at fixed impurity-bath coupling U_{ib}/t , the impurity localization is instead *compressibility-controlled*. Starting from a compressible SF bath, the impurity appears as a mobile light polaron with finite winding and an extended deformation cloud. As U_b/t increases, the bath superfluid density and compressibility are progressively suppressed and the impurity winding is continuously reduced. Upon entering the MI regime, the impurity crosses over to an almost free defect moving in a weakly distorted incompressible background with nearly flat deformation cloud, and in the deep MI phase its deformation cloud shrinks to within roughly two or three nearby sites, yielding a localized vacancy- or particle-like defect. This evolution is reflected in the impurity-centered cumulative bath density deformation $\Delta N(R)$, which changes from a broad polaronic profile in the SF to an almost flat response upon entering the MI, and eventually to a defect in the deep MI. In this way, the Letter established a global $U_b/t - U_{\text{ib}}/t$ phase diagram that connects light polarons, heavy polarons, and saturated-bubble/bound-cluster regimes for both signs of U_{ib}/t in the SF bath, as well as nearly free and fully localized defect states in the MI bath. It further clarified that, along interaction-driven trajectories in the SF, impurity localization occurs via a continuous crossover rather than a thermodynamic phase transition, whereas in the MI region it can become a sharp transition from a nearly free particle to a localized defect state, while at fixed U_{ib}/t the evolution of the impurity across the SF-MI boundary remains a smooth, compressibility-controlled crossover.

While the Letter [28] establishes a broad global picture of impurity localization in the Bose–Hubbard model, it does not fully develop a microscopic description of impurity behavior for attractive impurity–bath couplings, nor of impurity dynamics in genuinely *incompressible* Mott-insulating (MI) baths. In the MI regime of the Bose–Hubbard model, long-wavelength density fluctuations are gapped and the superfluid stiffness vanishes [?]. At weak U_{ib}/t , an impurity is expected to propagate almost as a free defect on top of a rigid background, while at strong $|U_{\text{ib}}|/t$ it should nucleate a localized particle- or hole-like defect, as suggested by Ref. [27]. The global phase diagram in our letter already indicated where interaction-driven winding-collapse and compressibility-controlled localization lines meet inside the MI region, but several key microscopic questions were left open: (i) How does the interaction-driven winding-collapse mechanism operate microscopically for attractive impurity–bath couplings in a superfluid background? (ii) Once the bath is strictly incompressible, to what extent do attractive and repulsive impurities exhibit qualitatively different localization patterns and deformation clouds? (iii) For a fixed attractive impurity-bath coupling, how does the compressibility-controlled localization proceed as the bath is tuned from the superfluid into the Mott-insulating regime?

In this paper, we build directly on the letter [28] and address

these questions by performing a systematic, numerically exact QMC study that focuses on attractive impurity–bath couplings and provides a detailed account of impurity behavior in Mott-insulating baths. We analyze three complementary trajectories. (i) In a compressible SF bath, we implement an *interaction-driven winding-collapse* protocol for attractive impurities by fixing the bath interaction at $U_b/t = 13.33$ and tuning U_{ib}/t from -1.0 to -40.0 , thereby following the evolution from a mobile light polaron with finite winding to a heavy polaron and then to a bound cluster while the bath remains globally superfluid. (ii) Inside the MI regime, we systematically compare attractive and repulsive impurity–bath couplings, revealing how nearly free defects and localized particle- or vacancy-like defects emerge as distinct localization patterns in an incompressible background. (iii) To expose the role of bath compressibility for attractive impurity, we implement a *compressibility-driven localization* protocol by fixing $U_{\text{ib}}/t = -8.0$ and tuning U_b/t from the deep SF regime, through the critical region, into the deep MI, tracking how the impurity winding and deformation cloud collapse as the bath turns incompressible. For each parameter set we measure the impurity winding number, the bath superfluid response and compressibility, as well as radial impurity-centered real-space correlator $C(R)$ and the cumulative bath-density deformation $\Delta N(R)$. Taken together with our companion Letter [28], these results turn the global picture of interaction-driven and compressibility-controlled localization into a fully microscopic description that covers both superfluid and Mott-insulating baths and both attractive and repulsive impurity–bath couplings.

Our results complement and extend previous work in several ways. First, by combining worldline winding diagnostics with radical impurity-centered real-space correlator $C(R)$ and cumulative bath-density deformation $\Delta N(R)$, we provide a direct visualization of the impurity’s localization process in both compressible SF and incompressible MI backgrounds, rather than inferring it solely from effective masses or ground state energy. Second, we clarify how interaction-driven winding collapse and compressibility-controlled localization operate at the microscopic level for attractive impurities: the same winding-based criterion, together with the deformation cloud, tracks the evolution from a mobile light polaron to a heavy polaron and finally to a bound cluster in the SF, and its subsequent modification as the bath loses compressibility. Third, by following the impurity across the SF–MI transition and into the deep MI regime, we show how the light polaron identified in the SF continuously evolves into a nearly free defect and then into a localized particle- or vacancy-like defect, thereby tying together the polaronic and defect descriptions within a single microscopic framework. Given the rapid experimental progress in site-resolved control of impurities in optical lattices [18–20], we expect that the observables and regimes identified here can be probed directly in future quantum-gas-microscope experiments.

The remainder of this paper is organized as follows. Section II introduces the two-component Bose–Hubbard Hamiltonian, and Sec. III describes the quantum Monte Carlo method and the definitions of single-impurity properties, bath observables, and impurity-centered quantities such as the impurity-

centered correlation $C_{\text{ib}}(\mathbf{r})$ and the cumulative bath-density deformation $\Delta N(R)$. Sections IV, V, and VI present our main numerical results. We first briefly summarize the overall impurity phase diagram previously established in [28], and then analyze in detail three complementary trajectories: (i) an interaction-driven winding-collapse path in a SF bath with attractive impurity-bath coupling U_{ib}/t , (ii) impurity physics in a Mott-insulating bath for representative attractive and repulsive couplings $U_{\text{ib}}/t = \pm 8.0$, and (iii) a compressibility-driven localization path where the bath is tuned from SF to MI at fixed $U_{\text{ib}}/t = -8.0$. For each case, we compare the evolution of the impurity winding number, the bath superfluid density response, and the impurity-centered real-space correlator $C(R)$ and its cumulative bath-density deformation $\Delta N(R)$. A summary of the main conclusions and an outlook are given in Sec. IX.

II. MODEL

We study a single mobile impurity immersed in a two-dimensional Bose–Hubbard bath on a square lattice described by the Hamiltonian

$$H = -t_{\text{imp}} \sum_{\langle i,j \rangle} (a_i^\dagger a_j + \text{H.c.}) + U_{\text{ib}} \sum_i n_{\text{imp},i} n_{\text{b},i} - t_{\text{b}} \sum_{\langle i,j \rangle} (b_i^\dagger b_j + \text{H.c.}) + \frac{U_{\text{b}}}{2} \sum_i n_{\text{b},i} (n_{\text{b},i} - 1) - \mu_{\text{b}} \sum_i n_{\text{b},i}, \quad (1)$$

where b_i^\dagger (a_i^\dagger) creates a bath (impurity) boson on lattice site i , and $n_{\text{b},i} = b_i^\dagger b_i$, $n_{\text{imp},i} = a_i^\dagger a_i$ are the corresponding on-site number operators. The bath hopping amplitude t_{b} sets the energy scale ($t_{\text{b}} = 1$ throughout), and the on-site repulsion U_{b} controls the superfluid–Mott insulator transition of the bath. The impurity hopping $t_{\text{imp}} = t = 1$ is taken equal to t_{b} . The local impurity–bath coupling U_{ib} is the key tuning parameter: $U_{\text{ib}} > 0$ corresponds to repulsion, $U_{\text{ib}} < 0$ to attraction. The bath chemical potential μ_{b} is adjusted to realize unit filling, while a single impurity is enforced by $\sum_i \langle n_{\text{imp},i} \rangle = 1$.

Physical regimes.— Figure 1 illustrates the contrast of a single impurity between a compressible superfluid (SF) bath and an incompressible Mott-insulating (MI) bath. In the SF regime, bath bosons (blue wavy lines) form a coherent condensate with long-range phase coherence. A repulsive impurity (red disk) pushes away nearby bath particles, creating a broad depletion cloud, while an attractive impurity draws in additional bath density, forming a smooth accumulation halo. Because the bath is compressible, these density modulations extend over many sites and the impurity exhibits coherent motion with finite winding. In the MI regime, density fluctuations are frozen and only local distortions survive. At smaller U_{b}/t , the impurity acts as a nearly-free defect for both repulsive and attractive impurity-bath couplings U_{ib}/t , while at larger U_{b}/t it turns into a localized defect: a vacancy defect on the repulsive side and a particle defect on the attractive side, both characterized by vanishing impurity winding.

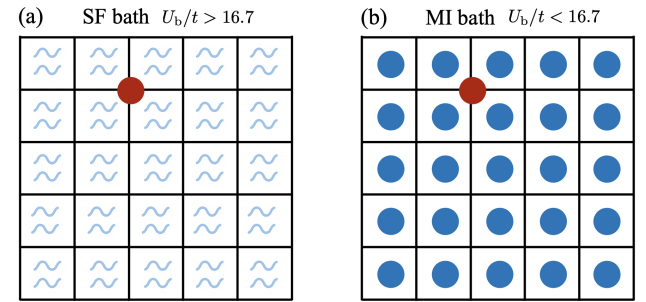


FIG. 1. **Schematic impurity behavior in superfluid (SF) and Mott-insulating (MI) baths.** The bath undergoes a SF–MI transition at $U_{\text{b}}/t \simeq 16.7$. (a) In a compressible SF bath, bosons (blue wavy background) possess long-range phase coherence and support extended density fluctuations. A repulsive impurity (red disk) creates a broad depletion cloud, whereas an attractive impurity induces a smooth accumulation halo. Because the bath is compressible, these density modulations spread over many sites and the impurity retains coherent motion with finite winding, forming a light polaron at weak coupling and an extended heavy state at stronger coupling. (b) In an incompressible MI bath, density fluctuations are frozen and only short-range particle–hole excitations are allowed. For both repulsive and attractive impurity–bath couplings, the impurity behaves as a nearly free defect at moderate U_{b}/t , producing only weak local distortion. At larger U_{b}/t the impurity becomes fully localized: a repulsive impurity expels one bath particle and forms a quantized vacancy defect, while an attractive impurity binds extra one boson into a particle defect. Both MI-side defects exhibit short-range density distortion and vanishing impurity winding, in stark contrast to the extended polaronic dressing in the SF regime.

We choose the chemical potential μ_{b} such that the homogeneous single-component Bose–Hubbard model (with $U_{\text{ib}}/t = 0$) is at unit filling. In the presence of a single impurity the bath is treated in the grand-canonical ensemble, so the total bath occupation deviates from unity only by an amount of order $1/L^2$, which is negligible for the thermodynamic properties discussed below. Throughout the paper we therefore refer to this situation as a unit-filled bath.

III. METHODS AND OBSERVABLES

We employ sign-problem-free multi-species worm-algorithm quantum Monte Carlo (QMC) in the path-integral representation. The method extends the original worm framework of Refs. [29, 30] to two bosonic species [31, 32]—impurity and bath—and samples their worldline configurations in imaginary time. Throughout this work we fix the impurity number to exactly one, i.e. the impurity is simulated in the canonical ensemble, while the bath bosons are treated in the grand-canonical ensemble with a chemical potential chosen to stabilize unit filling in the SF and MI regimes.

The algorithm introduces two independent worm operators that allow creation, moving, and annihilation of worldline discontinuities on each species, enabling efficient sampling

of both diagonal and off-diagonal correlators. Because the impurity interacts only via density–density terms and both species are bosonic, the method is strictly sign-problem free for all parameters studied here.

We simulate lattices up to $L = 20$ with periodic boundary conditions and use inverse temperatures $\beta = L$, which is sufficient to reach ground-state convergence in both the superfluid and the Mott-insulating regimes.

In the following, we summarize the observables used to characterize the impurity mobility and the accompanying bath deformation. All measurements are performed in the (canonical) single-impurity sector and in the grand-canonical ensemble for the bath, using the multi-species worm algorithm. Three global observables are central to our analysis. First, the impurity winding number $\langle W_{\text{imp}}^2 \rangle$ quantifies the coherent mobility of the impurity: a finite value signals a mobile light polaron, while its continuous suppression and eventual collapse indicate interaction-driven self-localization, ranging from heavy polarons and saturated bubbles or bound clusters in a superfluid bath to fully localized defects in a Mott-insulating bath. Second, the bath superfluid density ρ_s , obtained from the standard winding-number estimator, tracks the loss of global phase stiffness and thus diagnoses the SF–MI transition and the underlying bath compressibility. Third, impurity-centered density responses, encoded in the correlator $C_{\text{ib}}(\mathbf{r})$ and its cumulative bath-density deformation $\Delta N(R)$, resolve the real-space structure of the dressing cloud and distinguish depletion bubble, bound clusters, nearly free defect, and localized defect state. Statistical errors are estimated via jackknife analysis over independent Monte Carlo blocks, and radial profiles are smoothed by binning over shells of constant distance using the minimum-image convention.

A. Impurity weight and bath baseline

The bath density operator is $n_b(\mathbf{r})$, and the impurity occupation operator is $n_{\text{imp}}(\mathbf{r})$, which satisfies $\sum_{\mathbf{r}} \langle n_{\text{imp}}(\mathbf{r}) \rangle = 1$. Here \mathbf{r} labels lattice sites and is equivalent to the site index i used in Sec. II; sums over \mathbf{r} are therefore equivalent to sums over lattice sites. The impurity worldline may visit any site during imaginary time; its imaginary-time averaged spatial weight is defined as

$$w(\mathbf{r}_{\text{imp}}) = \frac{1}{\beta} \int_0^\beta \langle n_{\text{imp}}(\mathbf{r}_{\text{imp}}, \tau) \rangle d\tau, \quad \sum_{\mathbf{r}_{\text{imp}}} w(\mathbf{r}_{\text{imp}}) = 1. \quad (2)$$

The uniform bath density (baseline) is

$$\bar{n}_b = L^{-2} \sum_{\mathbf{r}} \langle n_b(\mathbf{r}) \rangle. \quad (3)$$

Spatial displacements are computed using the minimum–image convention under periodic boundary conditions.

In the worldline representation the impurity can wind around the periodic boundaries. We define the impurity winding vector $\mathbf{W}_{\text{imp}} = (W_{\text{imp}}^x, W_{\text{imp}}^y)$ as the net number of times the impurity worldline wraps around the system in the x and y

directions, respectively. As a scalar diagnostic we use

$$W_{\text{imp}}^2 \equiv (W_{\text{imp}}^x)^2 + (W_{\text{imp}}^y)^2, \quad (4)$$

and monitor $\langle W_{\text{imp}}^2 \rangle$ to distinguish between mobile and localized impurity regimes.

The bath superfluid density is obtained from the standard winding-number estimator. Denoting by $\mathbf{W}_b = (W_b^x, W_b^y)$ the winding numbers of the bath worldlines, we define $W_b^2 = (W_b^x)^2 + (W_b^y)^2$ and compute [33]

$$\rho_b = \frac{\langle W_b^2 \rangle}{2t_b \beta}, \quad (5)$$

for a two-dimensional system with lattice spacing set to unity.

The bath compressibility is measured from number fluctuations in the grand-canonical ensemble,

$$\kappa_b = \frac{\beta}{L^2} (\langle N_b^2 \rangle - \langle N_b \rangle^2), \quad N_b = \sum_{\mathbf{r}} \langle n_b(\mathbf{r}) \rangle. \quad (6)$$

Here κ_b vanishes in the incompressible MI regime and is finite in the SF.

Finally, we extract impurity quasiparticle properties from the single-impurity Green’s function measured in real space. Within the worm algorithm we sample

$$G_{\text{imp}}(\mathbf{r}, \tau) = \langle a_{\text{imp}}(\mathbf{r}, \tau) a_{\text{imp}}^\dagger(\mathbf{0}, 0) \rangle, \quad (7)$$

where \mathbf{r} is the spatial separation between the annihilation and creation operators. The momentum-resolved Green’s function is then obtained by a discrete Fourier transform over the lattice,

$$G_{\text{imp}}(\mathbf{k}, \tau) = \sum_{\mathbf{r}} e^{-i\mathbf{k} \cdot \mathbf{r}} G_{\text{imp}}(\mathbf{r}, \tau). \quad (8)$$

For sufficiently large imaginary time τ and low temperature, $G_{\text{imp}}(\mathbf{k}, \tau)$ is dominated by the lowest-lying impurity (polaron) state at momentum \mathbf{k} ,

$$G_{\text{imp}}(\mathbf{k}, \tau) \simeq Z_{\mathbf{k}} e^{-E_p(\mathbf{k}) \tau}, \quad (9)$$

where $E_p(\mathbf{k})$ is the polaron energy and $Z_{\mathbf{k}}$ is the quasiparticle residue. At $\mathbf{k} = \mathbf{0}$, fitting $G_{\text{imp}}(\mathbf{0}, \tau)$ to Eq. (9) yields the polaron ground-state energy $E_p(\mathbf{0})$ and residue Z_0 .

The effective mass is extracted from the small-momentum dispersion, $m^*/m_0 = \frac{2t}{\partial^2 E_p(\mathbf{k}) / \partial \mathbf{k}^2}$, where the curvature $\partial^2 E_p(\mathbf{k}) / \partial \mathbf{k}^2$ is obtained by fitting the lowest available momenta.

B. Impurity-centered correlator and radial averaging

We define the impurity-centered correlator as

$$G_{\text{ic}}(\mathbf{r}) = \sum_{\mathbf{r}_{\text{imp}}} w(\mathbf{r}_{\text{imp}}) \langle n_b(\mathbf{r}_{\text{imp}} + \mathbf{r}) \rangle, \quad (10)$$

$$C_{\text{ib}}(\mathbf{r}) = G_{\text{ic}}(\mathbf{r}) - \bar{n}_b. \quad (11)$$

Here \mathbf{r}_{imp} labels the lattice site occupied by the impurity, $C_{\text{ib}}(\mathbf{r})$ measures the change of bath density *conditioned* on the impurity location: $C_{\text{ib}}(\mathbf{r})/t < 0$ corresponds to depletion (repulsive $U_{\text{ib}}/t > 0$), while $C_{\text{ib}}(\mathbf{r})/t > 0$ corresponds to accumulation (attractive $U_{\text{ib}}/t < 0$).

To suppress lattice anisotropy we perform rotational averaging over shells of fixed Euclidean distance $R = |\mathbf{r}|$:

$$C_{\text{ib}}(R) = \frac{1}{N_R} \sum_{|\mathbf{r}|=R} C_{\text{ib}}(\mathbf{r}),$$

where N_R counts the sites satisfying $|\mathbf{r}| = R$ (using the minimum-image convention). This is identical to the definition used in our companion Letter [28].

C. Cumulative excess and its characteristic measures

The impurity-centered cumulative bath-density deformation, i.e., the net change of bath particle number within a distance R from the impurity, is defined as:

$$\Delta N(R) = \sum_{|\mathbf{r}| \leq R} C_{\text{ib}}(\mathbf{r}) = \sum_{R' \leq R} N_{R'} \bar{C}_{\text{ib}}(R'). \quad (12)$$

By construction $\Delta N(R \rightarrow \infty) = 0$ in the canonical ensemble (global particle number is fixed), while the behavior at small R reveals the local deformation created by the impurity.

In this work, we use two directly measurable quantities extracted from the cumulative profile.

(i) *Peak radius.* The radius at which the cumulative excess attains its extremum,

$$R(\Delta N_{\text{ext}}) = \begin{cases} \arg \min_R \Delta N(R), & U_{\text{ib}}/t > 0, \\ \arg \max_R \Delta N(R), & U_{\text{ib}}/t < 0, \end{cases} \quad (13)$$

provides a geometric estimate of the spatial extent of the depletion bubble for repulsive couplings and of the bound cluster for attractive couplings.

(ii) *Peak amplitude.* The extremal value itself,

$$\Delta N_{\text{ext}} = \begin{cases} \min_R \Delta N(R), & U_{\text{ib}}/t > 0, \\ \max_R \Delta N(R), & U_{\text{ib}}/t < 0, \end{cases} \quad (14)$$

quantifies the number of bath particles expelled or recruited by the impurity. For a saturated vacancy bubble, $\Delta N_{\text{ext}} \approx -1$; for a multi-particle bound cluster, $\Delta N_{\text{ext}} > 1$.

These two quantities, $R(\Delta N_{\text{ext}})$ and ΔN_{ext} , are exactly the ones plotted in Figs. 3, 6, 10, and 13. Together they provide a direct and unambiguous characterization of depletion-bubble and bound-cluster formation in both SF and MI baths.

D. On-site contrast

The most local indicator of the deformation is

$$C_{\text{ib}}(\mathbf{0}) = \langle n_{\text{b}}(\mathbf{r}_0) \rangle_{\text{imp}} - \bar{n}_{\text{b}}, \quad (15)$$

which captures the degree of on-site depletion (repulsive) or accumulation (attractive).

Together, $\langle W_{\text{imp}}^2 \rangle$, $C_{\text{ib}}(R)$, $\Delta N(R)$, and the extremal measures $\{R(\Delta N_{\text{ext}}), \Delta N_{\text{ext}}\}$ provide a detailed microscopic characterization of impurity dressing and localization in both the SF and MI phases and across the SF–MI transition.

IV. ATTRACTIVE IMPURITY IN A SUPERFLUID BATH: REAL-SPACE SELF-LOCALIZATION

In our companion Letter [28], we showed that, in a compressible superfluid bath at fixed $U_{\text{b}}/t = 13.3$, impurity localization is governed by an interaction-driven winding-collapse mechanism: as a repulsive impurity–bath coupling $U_{\text{ib}}/t > 0$ is increased, the impurity evolves from a mobile light polaron with finite winding and an extended dressing cloud to a heavy self-trapped state and, eventually, to a depletion saturated-bubble configuration with $\Delta N(R) \rightarrow -1$. In this section we turn to the attractive side. To reveal the mirror counterpart of the repulsive depleted bubble and to resolve the real-space structure of self-localization, we again fix the bath interaction at $U_{\text{b}}/t = 13.3$ (in the superfluid regime) and tune the attractive impurity–bath coupling $U_{\text{ib}}/t < 0$.

Quasiparticle properties along an interaction-driven trajectory. We start with the interaction-driven path in the superfluid bath and track how the impurity quasiparticle evolves as the attractive impurity–bath coupling is increased at fixed $U_{\text{b}}/t = 13.3$. Figure 2 shows the polaron energy E_{p}/t , the effective-mass ratio m^*/m_0 , and the residue Z as functions of $U_{\text{ib}}/t < 0$. For weak attraction $|U_{\text{ib}}|/t < 10.0$ the impurity forms a moderately dressed light polaron: the energy is only linearly shifted, the mass remains close to the bare value ($m^*/m_0 \approx 1\text{--}1.2$), and the residue is high, $Z \approx 1.0\text{--}0.6$. As $|U_{\text{ib}}|/t$ is increased, the energy drops almost linearly, the effective mass grows steadily to $m^*/m_0 \gtrsim 1.5$, and the residue is reduced to $Z \sim 0.2$, indicating progressively stronger dressing. Upon entering the strong-attraction regime $|U_{\text{ib}}|/t > 13.3$, the mass shows a sharp upturn while the residue is strongly suppressed, signaling the onset of an interaction-driven self-trapped cluster with very limited coherent mobility. This quasiparticle evolution is fully consistent with the winding-number collapse and the real-space contraction of the dressing cloud discussed in Figure 3 to 5, and together they establish a continuous crossover from a mobile light polaron at weak attractive impurity–bath coupling $|U_{\text{ib}}|/t$ to a heavy, nearly localized bound cluster at strong attraction in a still globally superfluid bath.

Attractive-branch dressing in a compressible superfluid bath. Figure 3 summarizes the real-space characteristics of the impurity dressing in the attractive branch, obtained at fixed bath interaction $U_{\text{b}}/t = 13.3$, well inside the superfluid regime. At weak coupling ($|U_{\text{ib}}|/t \lesssim 13.3$), $\Delta N(R)$ exhibits a broad, small-amplitude hump, indicating a light Bose polaron characterized by an extended dressing cloud and finite impurity winding. As the attraction strengthens ($13.3 \lesssim |U_{\text{ib}}|/t \lesssim 20.0$), the peak amplitude $\Delta N_{\text{max}}(R)$ grows, signaling a compression of the dressing cloud and the emergence of a heavy-polaron

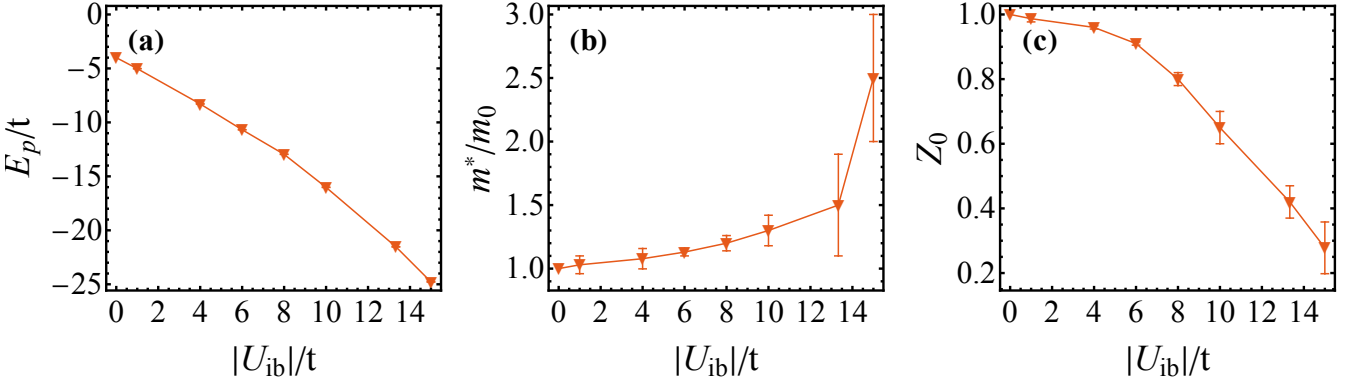


FIG. 2. **Quasiparticle properties of an attractive impurity in a superfluid bath.** (a) the polaron ground-state energy E_p/t , (b) the effective-mass ratio m^*/m_0 with m_0 the bare particle mass, and (c) the quasiparticle residue Z_0 as functions of the attractive impurity-bath coupling $|U_{ib}|/t$ at fixed bath interaction $U_b/t = 13.3$, deep in the superfluid regime. Error bars denote statistical uncertainties and are smaller than the symbols where not visible.

regime with reduced coherent mobility and nearly zero windings.

For stronger attractive impurity-bath coupling ($|U_{ib}|/t > 20.0$), the deformation cloud collapses toward the impurity site and $\Delta N(R)$ develops a sharply peaked profile at $R \simeq 2$, indicating the formation of a tightly bound multi-particle cluster. Unlike the repulsive saturated-bubble case, where the cumulative deficit $\Delta N(R)$ rapidly saturates at approximately -1 once R exceeds the depletion radius, here the cumulative excess ΔN_{\max} *continues to grow* with $|U_{ib}|/t$. Both branches are simulated in the same grand-canonical ensemble for the bath; the qualitative difference originates from the energetics of adding versus removing particles. For a repulsive impurity it is energetically favorable to expel essentially one bath boson from the impurity vicinity, producing a saturated depletion bubble with $\Delta N_{\min} \simeq -1$. For attractive $U_{ib}/t < 0$, the local potential well can instead bind several bath bosons: as $|U_{ib}|/t$ increases the optimal on-site occupation near the impurity grows to $C(R=0) \approx 3-4$ for our strongest couplings, so the bound cluster recruits a few extra particles from the reservoir. In a 20×20 system this corresponds to a total bath occupation of $N_b \simeq 403$, i.e., a global filling only slightly above unity, while the local excess is fully captured by the cumulative bath-density response $\Delta N(R)$. Taken together, these results establish the continuous crossover within the superfluid bath, *light polaron* \rightarrow *heavy polaron* \rightarrow *bound cluster*, all occurring while the bath remains globally superfluid.

In Fig. 4, we examine the impurity-centered correlation function $C_{ib}(R)$, which provides real-space insight into how the impurity distorts its local environment. The bath interaction is fixed at $U_b/t = 13.3$, well inside the superfluid phase, while the attractive impurity-bath coupling $U_{ib}/t < 0$ is tuned from weak to strong. For weak attraction ($|U_{ib}|/t \lesssim 13.3$, red curves), $C_{ib}(R)$ displays a shallow and spatially broad profile, reflecting a compressibility-enabled, extended dressing cloud characteristic of a coherent light polaron with finite winding and significant mobility, consistent with Fig. 5(a). In the intermediate regime ($13.3 < |U_{ib}|/t \lesssim 20$, yellow curves),

the correlation grows in amplitude while the winding has already collapsed to zero, signaling the formation of a compact heavy-polaron state with strongly reduced coherent motion. For strong attraction ($|U_{ib}|/t \gtrsim 20$, blue curves), all curves converge to a sharply peaked, nearly universal shape with a dominant on-site peak and a pronounced nearest-neighbor maximum, indicative of a tightly bound multi-particle cluster. The inset shows that the on-site signal $C_{ib}(0)$ increases *monotonically* with $|U_{ib}|/t$ and does not saturate. This behavior reflects the grand-canonical nature of the superfluid bath at fixed chemical potential: a deeper attractive potential can continuously recruit additional bath bosons into the cluster. It contrasts sharply with the repulsive branch, where the cumulative bath-density response $\Delta N(R)$ saturates at approximately -1 once a single bath particle has been expelled from the impurity vicinity.

Taken together, these results demonstrate a continuous, interaction-driven winding-collapse crossover from a coherent light polaron to a heavy polaron and finally a self-trapped, multi-particle bound cluster, even though the bath remains globally superfluid. The collapse of the spatial dressing profile thus provides a real-space signature of interaction-driven localization at fixed bath compressibility.

Winding-controlled localization of an attractive impurity in the superfluid bath. To directly probe how impurity mobility degrades with increasing attractive coupling, Fig. 5 summarizes the evolution of the impurity winding number $\langle W_{\text{imp}}^2 \rangle$ and the bath superfluid density ρ_b as a function of $U_{ib}/t < 0$ at fixed $U_b/t = 13.3$, deep in the compressible superfluid regime.

Figure 5(a) shows that $\langle W_{\text{imp}}^2 \rangle$ decreases smoothly at first, then rapidly collapses by nearly two orders of magnitude once $|U_{ib}|/t \gtrsim 13.3$, signaling a crossover from a mobile light polaron to a heavy polaron. This loss of winding takes place without any qualitative change in the bath, as confirmed in Fig. 5 (b), where the bath superfluid density ρ_b remains essentially constant across the entire range of impurity-bath couplings. The coexistence of vanishing impurity winding with a finite bath superfluid density clearly demonstrates that localiza-

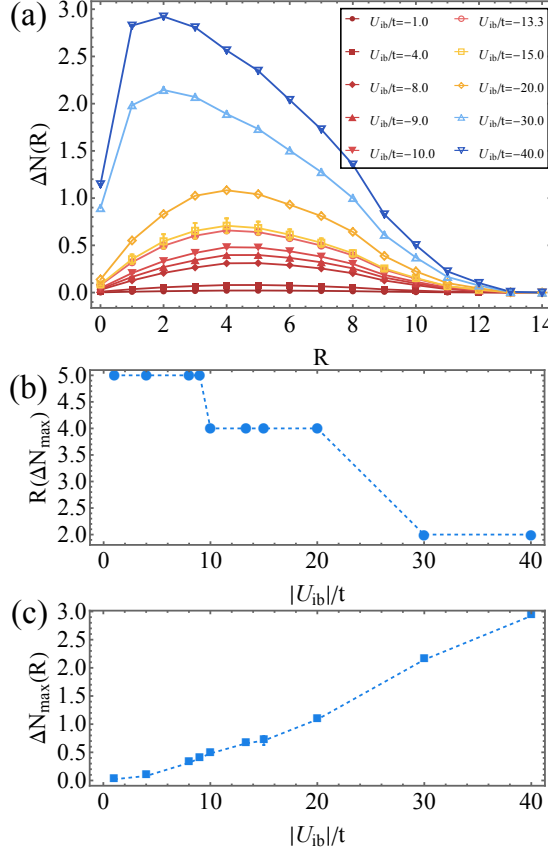


FIG. 3. **Real-space impurity dressing for attractive impurity in a superfluid bath at $U_b/t = 13.3$.** (a) Cumulative bath-density enhancement $\Delta N(R)$ for various attractive impurity-bath couplings $U_{ib}/t < 0$, showing the evolution from a broad, weak dressing cloud (light polaron) to a sharply localized multi-particle cluster. (b) Radius of the maximum $R(\Delta N_{\max})$, demonstrating the monotonic inward compression of the dressing cloud as $|U_{ib}|/t$ increases. (c) Magnitude of maximum $\Delta N_{\max}(R)$, which increases without saturation, reflecting the grand-canonical nature of the bath: stronger attraction continuously recruits additional bosons into the impurity vicinity. Unlike the repulsive saturated-bubble case where $\Delta N(R)$ saturates at -1 , the attractive branch exhibits unbounded growth due to unrestricted local accumulation. These results demonstrate a continuous crossover: light polaron \rightarrow heavy polaron \rightarrow bound cluster, while the bath remains globally superfluid.

tion is *not* driven by the breakdown of global phase coherence in the bath, but rather by an *interaction-driven winding collapse*, i.e., self-trapping of the impurity.

In contrast to a Mott-insulating background, where impurity localization involves quantized defect formation and abrupt expulsion or recruitment of a single bath boson, here the collapse of mobility is continuous. The bath remains fully superfluid and compressible, yet the impurity loses all long-range coherence and becomes localized purely by increasing the depth of the local attractive impurity-bath coupling. This establishes a clear case of *interaction-driven winding-collapse localization in a superfluid bath*: the impurity loses its ability to form worldline windings even though the bath retains macroscopic

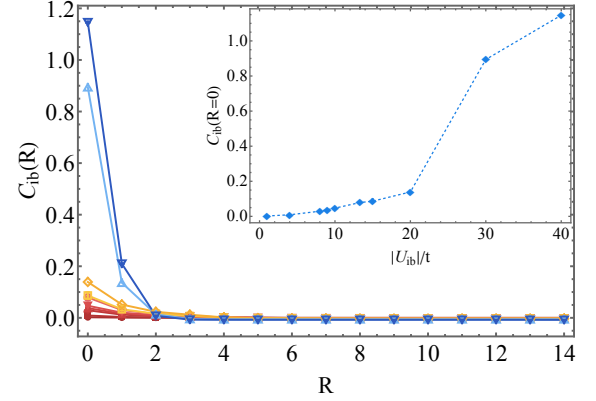


FIG. 4. **Real-space impurity-centered correlator $C_{ib}(R)$ in the superfluid bath at $U_b/t = 13.3$ for various attractive couplings $U_{ib}/t < 0$.** For weak attraction ($|U_{ib}|/t \lesssim 13.3$, red curves), $C_{ib}(R)$ is small and spatially broad, indicating an extended, compressible dressing cloud characteristic of a mobile light polaron. In the intermediate regime ($13.3 < |U_{ib}|/t \lesssim 20.0$, yellow curves), the response becomes stronger and short-ranged, signaling a compact heavy polaron with reduced coherent motion. For strong attraction ($|U_{ib}|/t > 20.0$, blue curves), the correlation collapses to a sharply peaked on-site form, forming a self-trapped, multi-particle bound cluster. The inset shows that the on-site value $C_{ib}(0)$ grows monotonically with $|U_{ib}|/t$ and does not saturate, highlighting that in a grand-canonical superfluid bath, a deeper attractive impurity continuously recruits additional bath bosons without intrinsic upper bound. This demonstrates an interaction-driven winding-collapse crossover in a compressible superfluid host.

superfluidity.

V. IMPURITY IN A MOTT-INSULATING BATH

Having established how the impurity evolves when the bath is in SF, we now turn to the complementary question: *What is the nature of the impurity once the bath is already deep in the Mott-insulating phase?* In this incompressible regime, long-wavelength density fluctuations are frozen and the superfluid density vanishes, removing the screening mechanisms that allow extended polarons to form in a compressible superfluid. Consequently, the impurity can perturb its environment only through strictly local rearrangements of bath occupation, in sharp contrast to the smooth, extended bath density deformations found in the SF regime.

A key feature of the Mott-insulator state is that bath occupation can change only in *integer* units. This quantization strongly constrains the impurity response: under a repulsive impurity-bath coupling ($U_{ib}/t > 0$), the impurity may lower its energy only by *expelling one* bath boson from its vicinity; under an attractive impurity-bath coupling ($U_{ib}/t < 0$), it may *recruit one* additional boson. Extended deformations, multi-particle halos, and continuous dressing clouds are forbidden by the incompressibility of the bath. Thus, impurity localization in the MI proceeds via discrete ± 1 -particle defects rather than via compressibility-enabled screening.

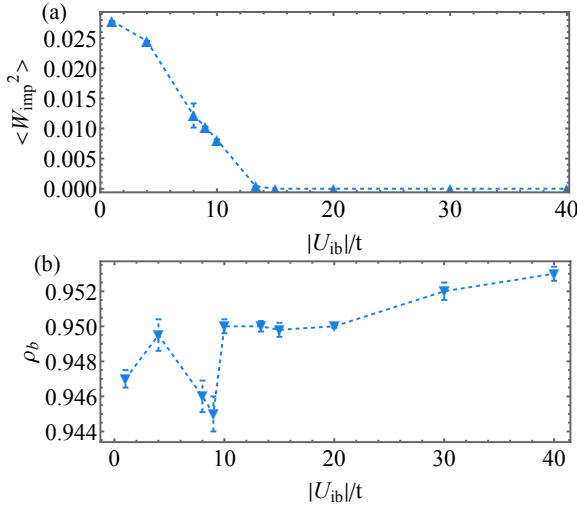


FIG. 5. **Interaction-controlled winding-collapse localization of an attractive impurity in a superfluid bath at fixed $U_b/t = 13.3$.** (a) Impurity winding number $\langle W_{\text{imp}}^2 \rangle$ as a function of attractive coupling $U_{\text{ib}}/t < 0$. A smooth suppression followed by a rapid collapse at $|U_{\text{ib}}|/t \gtrsim 10$ signals a transition from a mobile light polaron to a localized bound cluster. (b) Bath superfluid density ρ_b remains essentially unchanged across the entire coupling range, confirming that the impurity localization is *not* induced by the loss of global coherence in the bath. This establishes an interaction-driven winding-collapse localization mechanism: the impurity becomes localized even while the bath remains fully superfluid and compressible.

In the following two subsections we analyze these two cases separately at fixed bath interaction $U_b/t = 20.0$, representative of the deep Mott-insulating regime. For repulsive impurity-bath coupling, we show that the impurity evolves from a weakly dressed, nearly-free defect at small U_{ib}/t to a fully localized *vacancy defect* in which exactly one bath boson is expelled. For attractive impurity-bath coupling, we find an analogous progression from a lightly dressed defect to a localized *particle defect* that binds one additional boson.

Together, these two trajectories establish the characteristic, quantized signatures of impurity localization in an incompressible bath and highlight their fundamental difference from the continuous, bath interaction-driven dressing found on the superfluid side.

A. Repulsive impurity in a Mott-insulating bath

We now investigate the behavior of a repulsive impurity ($U_{\text{ib}}/t > 0$) embedded in a deep Mott-insulating bath with $U_b/t = 20.0$. In this regime, the background is incompressible, long-wavelength density fluctuations are frozen, and only local particle-hole excitations are accessible. Under these conditions the impurity cannot form an extended polaronic cloud: instead, its dressing is strictly local, and localization occurs through *discrete defect formation*. Figures 6–8 summarize our analysis.

Weak repulsion: nearly-free defect with minimal dressing. For repulsive impurity-bath couplings $U_{\text{ib}}/t \lesssim 12.0$, the im-

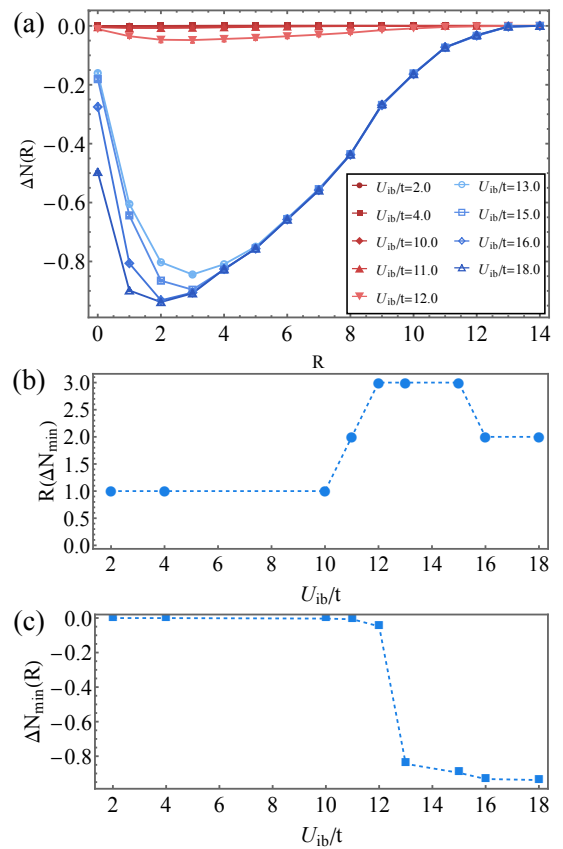


FIG. 6. **Repulsive impurity in a Mott-insulating bath: cumulative bath-density deformation.** (a) Cumulative bath-density deformation $\Delta N(R)$ for increasing repulsive coupling U_{ib}/t at $U_b/t = 20.0$. For weak U_{ib}/t , the response shows only a shallow minimum, indicative of a nearly-free defect. For $U_{\text{ib}}/t \gtrsim 13.0$, the minimum approaches $\Delta N_{\text{min}} \approx -1$, signaling the expulsion of a single bath particle. (b) Radius of the minimum, $R(\Delta N_{\text{min}})$, which sharply increases at the localization threshold. (c) Magnitude of the minimum $|\Delta N_{\text{min}}(R)|$, saturating to unity once the vacancy defect is formed.

purity behaves as a mobile, nearly-free defect propagating through the rigid Mott-insulating background. Figure 6(a) shows the cumulative bath response $\Delta N(R)$: the minimum ΔN_{min} is extremely shallow ($|\Delta N_{\text{min}}| \ll 0.02$), and its radius lies at $R(\Delta N_{\text{min}}) \approx 1\text{--}2$ sites, as quantified in Fig. 6(b). The impurity-centered correlator $C_{\text{ib}}(R)$ [Fig. 7(a)] exhibits only a small on-site dip with no visible tails, reflecting the short-range, weak rearrangement available in an incompressible background. The on-site contrast $C_{\text{ib}}(0)$ [inset of Fig. 7] remains near zero. Consistent with this picture, the impurity winding number $\langle W_{\text{imp}}^2 \rangle$ remains large and changes less than 10% [Fig. 8(a)], demonstrating that the impurity retains coherent mobility even in the absence of superfluidity of the bath.

Strong repulsion: formation of a localized vacancy defect. As U_{ib}/t increases beyond approximately 13.0, a sharp restructuring occurs in all observables. The cumulative bath-density deformation develops a deep, quantized minimum $\Delta N_{\text{min}} \approx -1$ [Fig. 6(c)], and the radius $R(\Delta N_{\text{min}})$ jumps

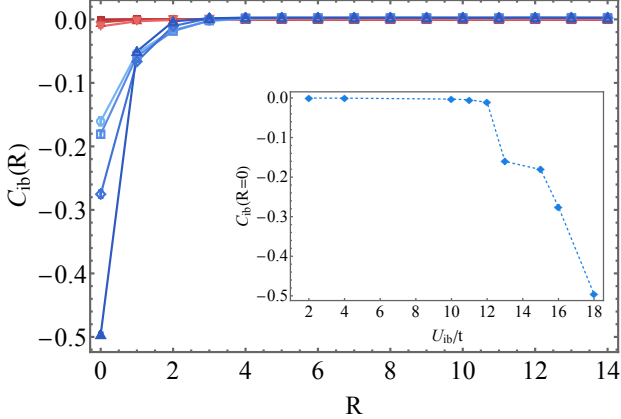


FIG. 7. **Repulsive impurity in a Mott-insulating bath: radial impurity-centered correlator.** Radical-averaged impurity-centered correlator $C_{ib}(R)$ evolves from a shallow, short-range dip at weak U_{ib}/t (nearly-free defect) to a deep on-site depletion with a compensating positive overshoot at larger R for $U_{ib}/t \gtrsim 12.0$, indicating formation of a saturated vacancy defect. *Inset:* on-site contrast $C_{ib}(0)$, showing a sharp drop at the same threshold, consistent with the expulsion of one bath particle from the impurity site.

to a larger value ≈ 2 or 3 [Fig. 6(b)]. These two signatures indicate that the impurity *expels exactly one* bath boson from its vicinity. The radial impurity-centered correlator $C_{ib}(R)$ develops a strongly negative on-site value and a small compensating positive overshoot at larger R [Fig. 7(a)]. Importantly, neither the magnitude $|\Delta N_{\min}|$ nor the overall profile changes with further increase of U_{ib}/t : the vacancy-defect formation is strictly quantized and fully saturated.

Coherence collapse and quantized particle loss. The vacancy-defect formation is accompanied by a collapse of coherent motion. The winding number $\langle W_{\text{imp}}^2 \rangle$ drops rapidly once $U_{ib}/t \simeq 13.0$ and approaches zero for larger impurity-bath couplings [Fig. 8(a)], signaling complete localization of the impurity–vacancy composite object. Simultaneously, the total bath particle number N_b decreases by *exactly one* particle [Fig. 8(b)], confirming that the impurity binds to a vacancy in the Mott-insulating background. This behavior is fundamentally distinct from the superfluid case discussed in companion: there, localization proceeds through a continuous redistribution of density, while in the Mott-insulating regime it is enforced by the discrete and gapped nature of particle–hole excitations. The impurity therefore transitions from a nearly-free defect to a fully localized vacancy defect as U_{ib}/t increases, providing a demonstration of defect-mediated localization in an incompressible quantum state.

B. Attractive impurity in a Mott-insulating bath

We now examine the opposite limit of an attractive impurity ($U_{ib}/t < 0$) embedded in the same Mott-insulating background with $U_b/t = 20.0$. Because the bath is incompressible, density redistribution cannot occur smoothly as in the SF case; instead, the impurity may only recruit bath bosons in discrete, integer

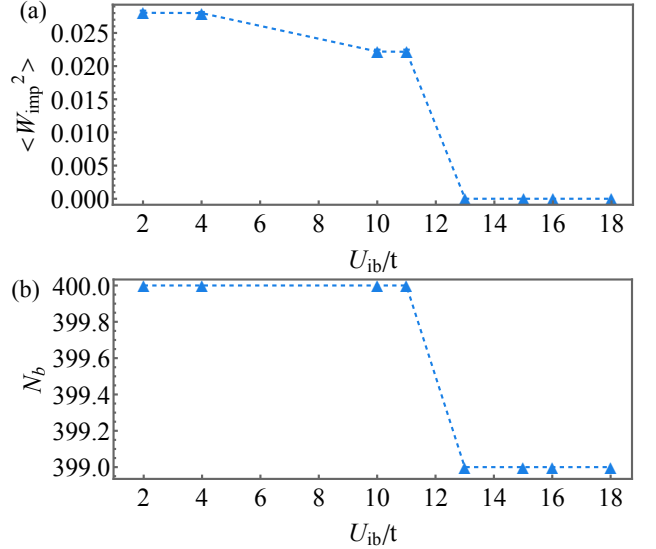


FIG. 8. **Impurity coherence and bath particle number for repulsive impurity-bath coupling in the MI.** (a) Impurity winding number $\langle W_{\text{imp}}^2 \rangle$. Finite winding at small U_{ib}/t confirms coherent motion of a nearly-free defect, whereas a rapid collapse when $U_{ib}/t > 13.0$ marks localization of the impurity–vacancy composite. (b) Total bath occupation N_b , showing a quantized decrease by exactly one particle once the vacancy defect is formed. This discrete change highlights that localization in the Mott-insulating regime proceeds by defect binding rather than extended density redistribution.

steps. Figures 9–11 summarize the evolution of the cumulative bath response, radial-averaged impurity-centered correlator, impurity coherence, and total bath occupation.

Weak attraction: nearly-free defect with minimal dressing. For $|U_{ib}|/t \lesssim 13.0$, the impurity behaves as a *nearly-free defect* in the MI background. The cumulative bath response $\Delta N(R)$ [Fig. 9(a)] displays only a small positive bump, with a shallow maximum $\Delta N_{\max} \ll 0.1$ located at $R(\Delta N_{\max}) \approx 4$ [Fig. 9(b)]. This indicates weak, short-range density attraction toward the impurity. Consistently, the radial-averaged impurity-centered correlator $C_{ib}(R)$ [Fig. 10] shows a modest on-site enhancement with negligible tail, and the on-site contrast $C_{ib}(0)$ (inset) remains close to zero. The impurity winding number $\langle W_{\text{imp}}^2 \rangle$ remains finite and only slowly decreases with increasing $|U_{ib}|/t$ [Fig. 11(a)], confirming that the impurity moves coherently through the rigid MI background. The total bath particle number N_b is pinned at its integer value [Fig. 11(b)], establishing that *no* bath particle has yet been trapped. Overall, the impurity forms only a weakly dressed defect, in sharp contrast to the extended droplets expected in a compressible superfluid environment.

Strong attraction: formation of a localized particle defect. A qualitative change occurs around $|U_{ib}|/t \simeq 13.0–14.0$. The cumulative bath response develops a rapidly growing positive maximum $\Delta N_{\max} \sim 1$ [Fig. 9(c)], while its position $R(\Delta N_{\max})$ remains confined to the first a few shells, $R \approx 1–3$ [Fig. 9(b)]. This indicates that the impurity abruptly binds an *integer* number of localized bath bosons—effectively one extra particle—into its vicinity, forming a compact particle-like

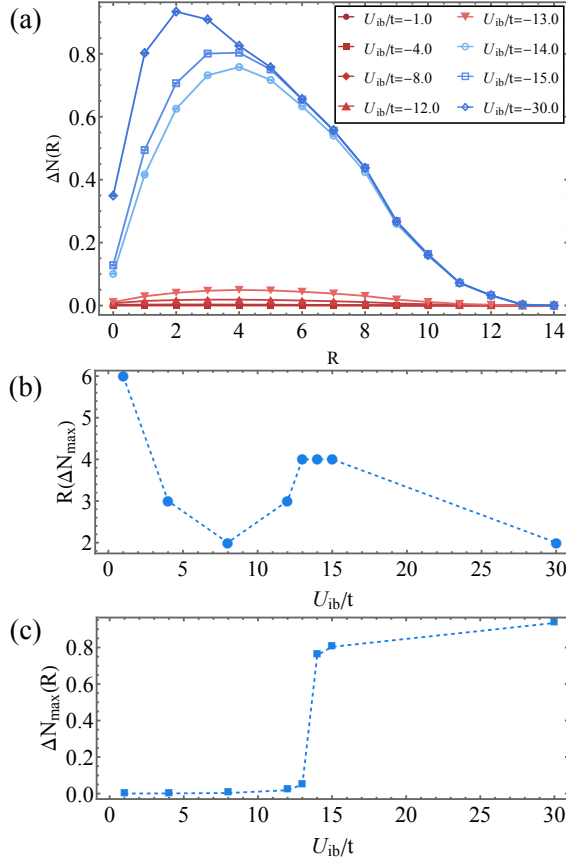


FIG. 9. **Attractive impurity in a Mott-insulating bath: cumulative bath-density deformation.** (a) Cumulative bath-density excess $\Delta N(R)$ for increasing attraction $|U_{ib}|/t$ at $U_b/t = 20.0$, showing the growth of a positive deformation near the impurity. (b) Radius of maximum, $R(\Delta N_{\max})$, extracted from panel (a). (c) Magnitude of maximum $\Delta N_{\max}(R)$. Its rapid increase to values $\gtrsim 2$ signals the recruitment of an integer number of bath bosons and the emergence of a localized particle-defect.

defect. The clustering is evident in the local correlator: $C_{ib}(0)$ increases sharply and reaches a large positive value [inset of Fig. 10], while the shape of $C_{ib}(R)$ shows a strong on-site accumulation followed by a tiny compensating negative tail, which restores global particle-number conservation. Beyond this threshold, further increasing $|U_{ib}|/t$ does not enlarge the accumulation cloud: the one-particle defect has fully saturated, and its spatial extent is limited by the on-site repulsion U_b/t of the Mott-insulating background.

Collapse of coherence and discrete particle recruitment. The formation of the particle-defect cluster is accompanied by a suppression of coherent impurity motion: $\langle W_{\text{imp}}^2 \rangle$ drops to zero for $|U_{ib}|/t \gtrsim 14.0$ [Fig. 11(a)]. Meanwhile, the total bath occupation N_{bath} increases by *exactly one* particle [Fig. 11(b)], demonstrating that the impurity binds to an additional bath boson to form a localized composite defect. This mechanism sharply contrasts with the smooth droplet formation in a superfluid bath. In the MI, the lack of compressibility forbids extended halos; localization proceeds through a *quantized* recruitment of bath particles.

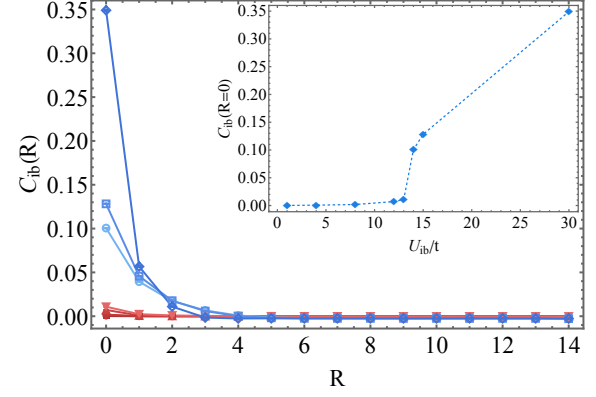


FIG. 10. **Attractive impurity in a Mott-insulating bath: radial impurity-centered correlator.** Radially averaged impurity-centered correlator $C_{ib}(R)$ for various $|U_{ib}|/t$, showing the evolution from a weak local enhancement (nearly-free defect) to a strong, sharply localized peak (particle-defect). Inset: on-site contrast $C_{ib}(0)$ versus U_{ib}/t , illustrating the abrupt growth of local density once the particle-defect formation threshold is crossed.

localized recruitment of bath particles. The resulting localized object is thus best viewed as a particle defect, distinct from both polarons (SF) and vacancy defect (repulsive MI).

Together, these results establish two characteristic regimes for attractive impurities in an incompressible bath: (i) a weakly dressed nearly-free defect at small $|U_{ib}|/t$; and (ii) a strongly bound, localized particle defect at larger $|U_{ib}|/t$, marked by discrete particle capture and vanishing impurity winding.

Contrast with the superfluid bath. In the compressible superfluid bath studied in Section IV the same impurity builds

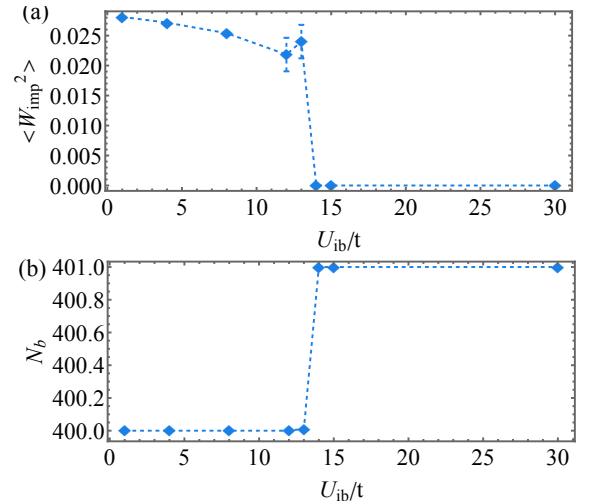


FIG. 11. **Impurity coherence and bath particle number for attractive impurity-bath coupling in the MI.** (a) Impurity winding number $\langle W_{\text{imp}}^2 \rangle$, showing finite mobility at small $|U_{ib}|/t$ (nearly-free defect) and a sharp suppression once a particle-defect forms. (b) Total bath particle number N_b . The discrete jump by one particle near $|U_{ib}|/t \approx 13.0$ –14.0 confirms the quantized recruitment of a bath boson and the formation of a localized composite defect.

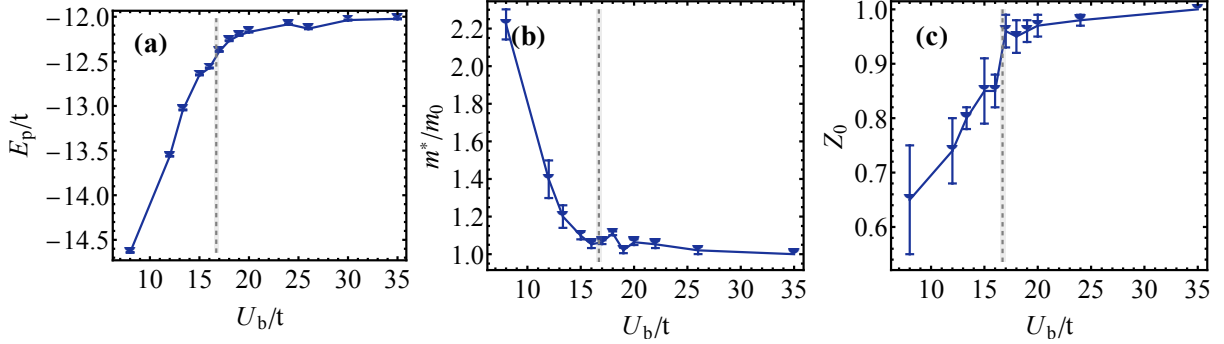


FIG. 12. **Quasiparticle properties of an attractive impurity across the SF-MI transition at fixed impurity-bath coupling $U_{\text{ib}}/t = -8.0$.** Ground-state energy E_p/t (a), inverse effective mass m^*/m_0 (b), and quasiparticle weight Z_0 (c) as functions of bath interaction U_b/t . The gray shaded band highlights the SF-MI crossover region ($U_b/t \approx 16.5$ –17.0). In the superfluid regime, the impurity behaves as a mobile light polaron with finite dressing cloud and moderate mass enhancement. As the bath approaches the SF-MI transition, both m^*/m_0 and Z_0 approach their bare values, reflecting the compressibility-controlled collapse of dressing. In the deep Mott-insulating regime, the impurity becomes a *nearly-free defect*, without forming a localized bound defect or recruiting an extra bath boson. Unlike the repulsive case at $U_{\text{ib}}/t = 8.0$, no quantized defect or vacancy/polaron complex is formed.

up a *continuous* accumulation halo as $U_{\text{ib}}/t \rightarrow -\infty$, with no quantized steps in the particle number. In the Mott-insulating bath considered here, by contrast, incompressibility prohibits extended dressing and enforces *discrete* recruitment of bath bosons once binding thresholds are crossed, leading to an integer increase in the local occupation and a concomitant collapse of coherent impurity motion.

VI. CROSSING THE SUPERFLUID–MOTT INSULATOR TRANSITION AT FIXED IMPURITY–BATH COUPLING

We now take a complementary viewpoint to the interaction-driven paths discussed above: instead of fixing the bath interaction U_b/t and varying impurity-bath coupling U_{ib}/t , we perform “vertical cuts” in the $(U_b/t, U_{\text{ib}}/t)$ plane by scanning the bath interaction U_b/t while keeping the impurity–bath coupling U_{ib}/t fixed. This strategy directly reveals how impurity properties evolve as the *bath medium* crosses the superfluid–Mott insulator transition, and allows us to isolate the role of bath compressibility from that of the impurity–bath coupling strength itself.

We begin with the representative intermediate attractive impurity-bath coupling $U_{\text{ib}}/t = -8.0$, which in a superfluid bath lies close to the self-trapping threshold identified in the phase diagram of our companion Letter [28]. This choice provides an ideal starting point to trace how the impurity’s coherence, mobility, and dressing cloud collapse as the bath loses compressibility: as U_b/t is increased from the deep-superfluid regime ($U_b/t = 8.0$ –16.0), through the critical region ($U_b/t \simeq 16.7$), and into the Mott-insulating regime ($U_b/t = 17.0$ –24.0), the impurity evolves from a well-defined light polaron in the SF to a nearly free defect in the MI.

Overview and observables. Along this compressibility-driven trajectory at fixed $U_{\text{ib}}/t = -8.0$, we monitor both quasiparticle-level and bath-level quantities. On the impurity side we extract (i) the ground-state energy E_p , (ii) the effective

mass m^*/m_0 from the single-impurity Green’s function, (iii) the quasiparticle residue Z_0 , and (iv) the impurity winding-number estimator $\langle W_{\text{imp}}^2 \rangle$, which directly quantifies the extent of coherent motion and serves as our primary marker of localization. On the bath side we measure (i) the superfluid density ρ_s from global winding statistics, which tracks macroscopic phase coherence and stiffness, and (ii) the radial-averaged impurity-centered density response encoded in $C_{\text{ib}}(R)$ and its cumulative bath-density deformation $\Delta N(R)$, which reveal the range, sign, and degree of quantization of the dressing cloud. Taken together, these observables provide a unified microscopic picture linking global coherence, local density structure, and quasiparticle properties across the compressibility-controlled SF–MI transition.

In contrast to the repulsive case analyzed in the companion Letter [28], where a moderate repulsion $U_{\text{ib}}/t = +8.0$ drives the impurity into a fully localized defect in a deep Mott-insulating background. We now examine the attractive case at fixed impurity–bath coupling $U_{\text{ib}}/t = -8.0$, and vary the bath interaction U_b/t across the superfluid–Mott insulator transition. This vertical trajectory is qualitatively different from the repulsive one: because the attraction is moderate and the bath becomes increasingly incompressible as U_b/t increases, the impurity can no longer sustain a heavy polaron nor form a bound cluster with multiple bath bosons. Instead, its dressing cloud continuously shrinks, and ultimately the impurity crosses over into a nearly-free defect even in the deep Mott-insulating regime. Importantly, at this coupling strength the impurity *never becomes a localized defect and never recruits an additional bath particle*; it remains mobile, with only minimal local density distortion.

Quasiparticle properties across the SF–MI transition. Figure 12 shows the evolution of the ground-state energy E_p/t , inverse effective mass m^*/m_0 , and quasiparticle residue Z_0 as functions of U_b/t . In the superfluid regime ($U_b/t \lesssim 16.0$), the impurity behaves as a light polaron characterized by extended density accumulation, moderately enhanced mass

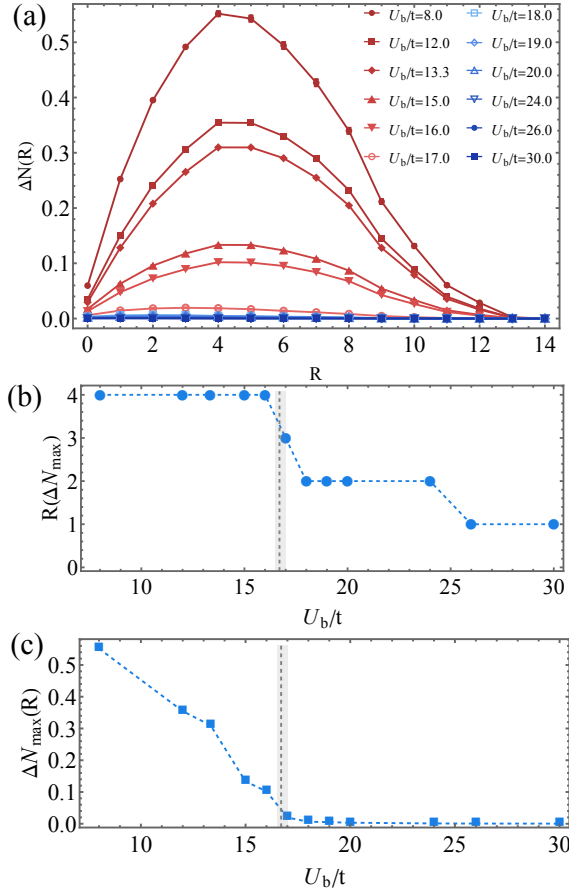


FIG. 13. Real-space impurity dressing for attractive impurity across the SF-MI transition at fixed attractive impurity-bath coupling $U_{ib}/t = -8.0$. (a) Cumulative bath-density deformation $\Delta N(R)$ for increasing U_b/t . In the superfluid regime ($U_b/t \lesssim 15.0$), the impurity generates an extended accumulation halo with maximum $\Delta N_{\max} \approx 0.5$ at $R \approx 4$, characteristic of a light polaron with finite spatial dressing. As the bath approaches the SF-MI critical region ($U_b/t \sim 16.7$), both the amplitude and width of the halo collapse, reflecting the suppression of compressibility and the disappearance of long-range screening. Inside the Mott-insulating regime ($U_b/t_b \gtrsim 18.0$), $\Delta N(R)$ becomes almost flat with $\Delta N_{\max} \lesssim 0.02$ and $R(\Delta N_{\max}) = 1$, indicating a purely local, short-range distortion without real particle recruitment. (b) Radius of maximum $R(\Delta N_{\max})$ rapidly drops from $R \approx 4$ in the superfluid to $R = 1$ in the Mott insulator phase, confirming that dressing becomes strictly local once compressibility vanishes. (c) Magnitude of maximum ΔN_{\max} with increasing U_b/t . Its smooth decay and nearly zero value demonstrate that the impurity remains a weakly dressed, nearly-free defect, never reaching the particle defect regime for this impurity-bath coupling strength $U_{ib}/t = -8.0$.

$m^*/m_0 \simeq 1.1\text{--}2.5$, and quasiparticle weight $Z_0 \simeq 0.7\text{--}0.9$. As the bath becomes less compressible and approaches the critical region ($U_b/t \approx 16.7$, shaded band), both m^*/m_0 and Z_0 rapidly approach their bare values, reflecting a compressibility-controlled collapse of polaronic dressing. Deep in the Mott-insulating regime ($U_b/t \geq 18.0$), bath density fluctuations are frozen, and the impurity behaves as a nearly-free defect with $m^*/m_0 \approx 1$, $Z \rightarrow 1$, and only a small, strictly local density

enhancement.

Bath responses across the SF-MI transition. Figure 13(a) shows the impurity-centered cumulative bath-density deformation $\Delta N(R)$ for a sequence of increasing U_b/t at fixed $U_{ib}/t = -8.0$. In the superfluid regime $U_b/t \lesssim 16.0$, the impurity induces a smooth, spatially extended density *accumulation halo*, with a broad maximum $\Delta N_{\max} \approx 0.5$ located at $R \approx 4$. This reflects a light polaron with coherent mobility and an extended dressing cloud. As U_b/t approaches the SF-MI critical region ($U_b/t \approx 16.7$), both the amplitude ΔN_{\max} and the radius $R(\Delta N_{\max})$ shrink rapidly [Figs. 13(b,c)], signaling a *compressibility-controlled collapse* of extended dressing: the halo can no longer spread through an increasingly rigid bath.

Inside the Mott-insulating regime ($U_b/t \gtrsim 18.0$), $\Delta N(R)$ becomes almost flat, with $\Delta N_{\max} \lesssim 0.02$ and $R(\Delta N_{\max}) = 1$ or 2, indicating that the impurity induces only a very weak, short-range density enhancement confined to its vicinity. The tiny amplitude confirms the absence of real particle recruitment: no additional bosons are bound to the impurity, and thus no bound cluster or multi-particle defect forms. Instead, the impurity remains a *nearly free defect* propagating in an essentially rigid background. Thus for $U_{ib}/t = -8.0$ the impurity never crosses into a localized particle-defect regime, even deep inside the Mott insulator phase.

These observations provide an important contrast to the repulsive case at similar impurity-bath coupling $U_{ib}/t = 8.0$ in MI bath, where a vacancy defect emerges once the bath becomes incompressible. For attractive $U_{ib}/t = -8.0$, the impurity is energetically unable to attract and bind a full additional boson because of the large interaction gap of the Mott insulator; the local distortion remains bounded by $|\Delta N_{\max}| < 0.02$, and no quantized particle capture or cluster formation occurs. The resulting state is therefore a weakly dressed, nearly free defect, consistent with the vanishing bath compressibility and strong on-site repulsion.

Figure 14 further characterizes the radical-centered impurity-bath correlator $C_{ib}(R)$ along the vertical cut at fixed $U_{ib}/t = -8.0$. The radial-averaged correlator $C_{ib}(R)$ in the main panel shows a pronounced on-site accumulation in the weakly interacting superfluid ($U_b/t = 8.0$), followed by a broad positive tail, consistent with the extended density halo seen in $\Delta N(R)$ and indicative of a light polaron with substantial bath dressing. As U_b/t increases toward the SF-MI boundary, both the amplitude and the range of $C_{ib}(R)$ are continuously suppressed, reflecting the compressibility-controlled collapse of the dressing cloud: an increasingly rigid bath can no longer support long-ranged density redistribution.

Once the bath enters the Mott-insulating regime ($U_b/t \gtrsim 17.0$), $C_{ib}(R)$ becomes extremely short-ranged and decays to zero within one lattice spacing. The inset highlights the on-site contrast $C_{ib}(0)$, which decreases monotonically with U_b/t and reaches $|C_{ib}(0)| \lesssim 10^{-3}$ for $U_b/t > 22.0$. This tiny local signal confirms that, for $U_{ib}/t = -8.0$, the impurity does not bind any additional bath bosons in the Mott insulator phase: no quantized particle defect is formed, and the impurity remains a weakly dressed, nearly free defect embedded in an incompressible background. This behavior stands in sharp contrast to the stronger-attraction regime ($|U_{ib}|/t \gtrsim 12.0$)

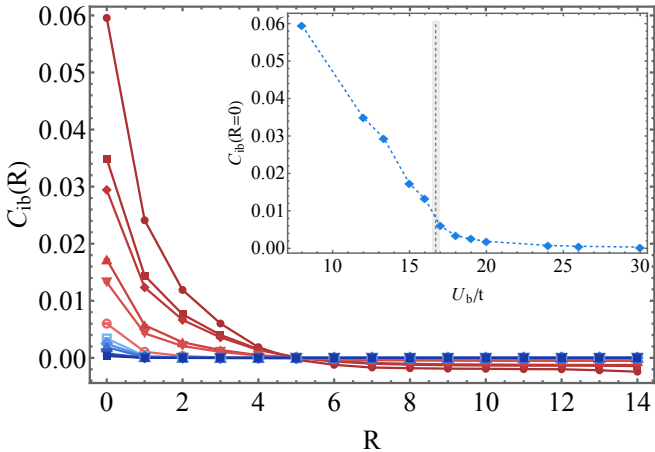


FIG. 14. Radial-averaged impurity-centered correlator $C_{ib}(R)$ at fixed attractive coupling $U_{ib}/t = -8.0$ across SF-MI transition. Main panel: Radial impurity-centered correlator $C_{ib}(R)$ for different bath interactions. In the superfluid regime ($U_b/t = 8.0-12.0$), $C_{ib}(R)$ shows a smooth, extended positive halo, characteristic of a mobile light polaron. As U_b/t increases, both the amplitude and range of $C_{ib}(R)$ are continuously suppressed, demonstrating the compressibility-driven collapse of bath dressing. In the deep Mott-insulating regime ($U_b/t \geq 22.0$), the correlator becomes strictly short-ranged and nearly vanishes, indicating the formation of a *nearly-free defect* with no particle-defect formation. Inset: On-site contrast $C_{ib}(0)$ as a function of U_b/t . Its monotonic decay to nearly zero confirms that, at moderate attraction ($U_{ib}/t = -8.0$), the impurity never recruits one additional bath boson and does not form a localized particle-defect, in contrast to the strong-attraction case discussed elsewhere.

discussed in Sec. V B, where a quantized particle-defect with $\Delta N_{\max} \gtrsim 1$ is stabilized in the MI phase.

The winding estimator of the impurity and bath-superfluid density in Fig. 15 provide a complementary view of the same compressibility-controlled crossover. In the superfluid regime the impurity winding $\langle W_{\text{imp}}^2 \rangle$ is clearly finite, consistent with a mobile light polaron dressed by an extended density halo. As U_b/t is increased and the bath superfluid density ρ_b collapses at the SF-MI transition, the winding increases even for the largest U_b/t considered. This confirms that, for $U_{ib}/t = -8.0$, the impurity evolves into a nearly free defect whose weak residual dressing is captured by the small but finite cumulative bath-density deformation in $\Delta N(R)$ and the short-ranged correlator $C_{ib}(R)$.

VII. SUMMARY OF MAIN RESULTS

Taken together, our results provide a unified microscopic picture of how a single impurity localizes in the two-dimensional Bose–Hubbard model when the impurity–bath coupling is attractive. Along the interaction-driven trajectory in a fixed superfluid bath ($U_b/t = 13.3$), increasing $|U_{ib}|/t$ drives a continuous winding-collapse crossover from a mobile light polaron with an extended dressing cloud, to a compact heavy polaron, and finally to a tightly bound multi-particle cluster. This evolu-

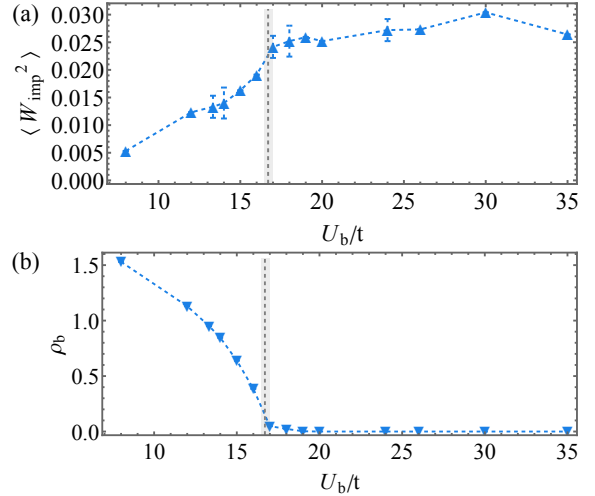


FIG. 15. Compressibility-controlled localization of an attractive impurity across the SF-MI transition with fixed impurity-bath coupling $U_{ib}/t = -8.0$. (a) Impurity winding-number estimator $\langle W_{\text{imp}}^2 \rangle$ as a function of bath interaction U_b/t . In the superfluid regime ($U_b/t < 16.7$), $\langle W_{\text{imp}}^2 \rangle$ is finite, indicating a mobile light polaron. Across the SF-MI transition the winding increases even deep in the Mott insulator phase, showing that the impurity crosses over to a nearly free defect rather than a fully localized particle-defect. (b) Bath superfluid density ρ_b extracted from global winding statistics, demonstrating the loss of phase stiffness across the superfluid–Mott insulator transition. The collapse of ρ_b correlates with the suppression of compressibility-enabled dressing, while the finite $\langle W_{\text{imp}}^2 \rangle$ in panel (a) highlights the persistence of coherent impurity motion in the Mott-insulating regime.

tion is captured consistently by the winding number estimator of the impurity, the real-space impurity-centered correlators $C_{ib}(R)$ and cumulated bath-density deformation $\Delta N(R)$, and the quasiparticle parameters E_p , m^*/m_0 , and Z_0 : the winding on the impurity is suppressed, the cloud contracts, the effective mass grows, and the residue is strongly reduced while the bath remains globally superfluid.

In the Mott-insulating regime, incompressibility qualitatively reshapes the impurity physics. For sufficiently strong repulsive and attractive couplings, the impurity nucleates quantized vacancy- and particle defect, respectively: the impurity winding collapses, $\Delta N(R)$ saturates at integer values (e.g., $\Delta N_{\max} \simeq -1$ for a vacancy and $\Delta N_{\max} \gtrsim 1$ for a bound cluster), and the deformation becomes confined to within one or two lattice spacings. The impurity thus turns into a fully localized defect, and the Mott-insulating bath accommodates it by carrying an integer particle deficit or surplus in its vicinity, directly reflecting the incompressibility and interaction gap of the Mott-insulating background.

A complementary viewpoint is provided by compressibility-controlled trajectories at fixed impurity–bath coupling, exemplified here by the intermediate attraction $U_{ib}/t = -8.0$. As the bath interaction U_b/t is increased from the deep-superfluid regime, through the critical region, and into the Mott insulator phase, the bath superfluid density and compressibility collapse and the extended density halo around the impurity shrinks

and eventually disappears. At the same time, the impurity winding increases and the deformation amplitude $|\Delta N_{\max}|$ is smaller than 0.02, with no quantized vacancy or cluster formation. Along such trajectories, impurity localization is therefore governed by a purely compressibility-controlled suppression of coherent dressing, and the impurity crosses over from a light polaron in a compressible superfluid bath to a weakly dressed, nearly free defect in an incompressible Mott insulator. The comparison of these regimes highlights that impurity localization in the Bose–Hubbard model can proceed either via interaction-driven winding-collapse in a superfluid bath, or via a compressibility-controlled collapse of polaronic dressing when the bath is tuned across the SF–MI transition.

VIII. EXPERIMENTAL REALIZATION

The two-component Bose–Hubbard Hamiltonian in Eq. (1) can be implemented with state-of-the-art ultracold bosonic mixtures in optical lattices. A natural realization uses two hyperfine states of ^{87}Rb or ^{41}K loaded into a square optical lattice, where one component (the bath) realizes a Bose–Hubbard system with a tunable ratio U_b/t_b controlled by the lattice depth and scattering length [13, 17, 34, 35]. A dilute population of atoms in a second hyperfine state then plays the role of mobile impurities with tunneling amplitude t_{imp} and an on-site interaction U_{ib} with the bath species.

The impurity–bath coupling U_{ib} can be tuned in both magnitude and sign using interspecies Feshbach resonances in bosonic mixtures, providing access to the repulsive and attractive regimes discussed in this work [36]. Independent control of the impurity hopping t_{imp} is achievable with species-selective or state-dependent optical lattices, which engineer different lattice depths for the two components and thus realize tunable ratios t_{imp}/t_b [37, 38]. Within these established techniques, the parameter ranges explored in our QMC simulations—covering superfluid and Mott-insulating baths and intermediate impurity–bath couplings—are well matched to those already realized in current experiments on lattice bosons.

Single-site-resolved imaging with quantum gas microscopes provides direct access to the real-space observables introduced in this work [18–20]. In particular, the impurity-centered correlator $C_{\text{ib}}(\mathbf{R})$ can be reconstructed from conditional density maps by post-selecting snapshots in which the impurity is found at position \mathbf{r}_{imp} and averaging the bath occupation at $\mathbf{r}_{\text{imp}} + \mathbf{R}$. Radial integration of these maps yields the cumulative deformation $\Delta N(R)$, directly visualizing the formation of depletion bubbles or bound clusters around the impurity. Moreover, repeated preparation and readout of the impurity trajectory would allow one to access winding-number statistics and thereby probe the crossover from coherent motion to localized defects.

Taken together, the combination of tunable lattice depth, controllable interspecies interactions, and single-site readout provides a realistic experimental route to explore all impurity regimes identified in our QMC study: from mobile light polarons through heavy polarons to saturated bubbles (for re-

pulsive impurity–bath couplings) or bound clusters (for attractive couplings) in the superfluid bath, and from nearly free defects to fully localized vacancy- or particle-like defects in the Mott-insulating regime.

IX. DISCUSSION AND OUTLOOK

The present work provides a unified microscopic picture of impurity localization across compressible superfluid phase and incompressible Mott-insulator phase within the two-dimensional Bose–Hubbard model. By combining worldline winding diagnostics with real-space bath deformations, we have established that the impurity localization phenomenon is in fact controlled by two distinct mechanisms depending on the bath compressibility and impurity–bath coupling.

In the superfluid regime, where long-wavelength phase fluctuations are gapless and the bath remains fully compressible, the buildup of dressing is a continuous process. As impurity–bath coupling $|U_{\text{ib}}|/t$ is increased at fixed U_b/t , the impurity’s winding number and the associated coherent motion are gradually suppressed: the winding estimator of the impurity decreases and eventually collapses as the impurity approaches a self-trapped regime. In parallel, the cumulative bath density deformation $\Delta N(R)$ evolves smoothly from a weak, extended halo, shown by a broad, low-amplitude $C_{\text{ib}}(R)$, to a compact, high-contrast structure in which the response $C_{\text{ib}}(R)$ is concentrated within one or two lattice spacings. On the repulsive side, this limiting configuration corresponds to a saturated depletion bubble with $\Delta N_{\max} \simeq -1$, whereas on the attractive side it becomes a dense bound cluster with $\Delta N_{\max} \gtrsim 1$. Throughout this evolution the bath remains globally superfluid, so the localization is controlled entirely by the interaction-driven collapse of winding and dressing, rather than by any loss of phase coherence in the bath.

In contrast, in the Mott-insulating regime, the situation changes qualitatively. The bath becomes incompressible, long-wavelength fluctuations are frozen, and only local particle–hole excitations with discrete energies remain. The impurity can no longer dress itself continuously; instead, localization proceeds through the formation of quantized density defects: for repulsive coupling, a single bath boson is expelled from the impurity vicinity, producing a vacancy-defect with $N_{\min} \approx -1$; for attractive coupling, one boson is captured to form a particle-defect with $N_{\max} \approx 1$. These two regimes represent mirror images of each other, illustrating how the sign of impurity–bath coupling U_{ib}/t determines whether the impurity locally depletes or enriches the background. The jump in $\langle W_{\text{imp}}^2 \rangle$, together with the discrete jump in local bath occupancy, demonstrates that the impurity’s coherence vanishes abruptly and the underlying density response is quantized. This dual behavior embodies the interplay between quantum coherence and the integer-filling constraint of the Mott insulator state.

From a broader perspective, our results suggest that a single impurity acts as a local quantum probe of the many-body gap. The correlations between the impurity winding, the extremal cumulative deformation ΔN_{ext} (either ΔN_{\min} or ΔN_{\max}), and the global bath compressibility provide a sensitive diag-

nostic of the onset of incompressibility: as the gap opens, the winding collapses and the integrated density deviation becomes quantized. This type of impurity-based diagnosis is conceptually similar in spirit to local spectroscopy and impurity thermometry in quantum gases, but is realized here entirely within an equilibrium path-integral framework. The same observables could be measured directly using site-resolved quantum gas microscopy: $C_{ib}(R)$ can be extracted from conditional density maps averaged over snapshots in which the impurity occupies site \mathbf{r}_{imp} , while the cumulative bath-density response $\Delta N(R)$ can be reconstructed from the radially averaged impurity-centered correlator $C_{ib}(R)$. Tracking the impurity trajectory over repeated experimental runs would give access to the winding-number statistics and hence to the crossover from mobile to localized regimes.

Several extensions of this work naturally arise. First, finite-temperature effects may reveal the thermal activation of particle-hole excitations in the Mott-insulating background, leading to a temperature-dependent delocalization crossover. Second, by introducing multiple impurities, one can study induced inter-

actions mediated by the bath, ranging from weak RKKY-like coupling in the superfluid to bound “defect pairs” in the Mott insulator. Third, relaxing the constraint $t_a = t_b$ introduces an additional tuning knob: in the limit $t_a \ll t_b$ the impurity becomes effectively heavy, approaching the static defect problem, whereas $t_a \gg t_b$ realizes a fast impurity moving through a slow, strongly correlated bath, allowing comparison with nonequilibrium polaron dynamics. Finally, by focusing on the two-impurity sector one can address bipolaron formation directly. Even in the simplest case without explicit impurity-impurity interactions, bath-mediated attraction may bind two impurities into a composite object whose binding energy and effective mass can be mapped across the $(U_{ib}/t, U_b/t)$ plane. Including a tunable direct impurity-impurity coupling would further allow one to disentangle bath-mediated and bare interactions, and remains fully accessible within the same sign-problem-free QMC framework.

Acknowledgments— We are grateful to Guido Pupillo for bringing this idea to our attention and for helpful discussions. We thank Nikolay Prokof’ev for insightful discussions.

[1] F. Grusdt, N. Mostaani, E. Demler, and L. A. P. Ardila, Impurities and polarons in bosonic quantum gases: a review on recent progress, *Reports on Progress in Physics* **88**, 066401 (2025).

[2] F. Scazza, M. Zaccanti, P. Massignan, M. M. Parish, and J. Levinsen, Repulsive fermi and bose polarons in quantum gases, *Atoms* **10**, 10.3390/atoms10020055 (2022).

[3] L. A. Peña Ardila and S. Giorgini, Impurity in a Bose–Einstein condensate: Study of the attractive and repulsive branch using quantum Monte Carlo methods, *Physical Review A* **92**, 033612 (2015).

[4] L. A. Peña Ardila and S. Giorgini, Bose polaron problem: Effect of mass imbalance on binding energy, *Physical Review A* **94**, 063640 (2016).

[5] L. A. Peña Ardila, N. B. Jørgensen, T. Pohl, S. Giorgini, G. M. Bruun, and J. J. Arlt, Analyzing the Bose polaron across resonant interactions, *Physical Review A* **99**, 063607 (2019).

[6] L. A. Peña Ardila, G. M. Astrakharchik, and S. Giorgini, Strong-coupling Bose polarons in a two-dimensional gas, *Physical Review Research* **2**, 023405 (2020).

[7] N.-E. Guenther, P. Massignan, M. Lewenstein, and G. M. Bruun, Bose polarons at finite temperature and strong coupling, *Phys. Rev. Lett.* **120**, 050405 (2018).

[8] Y. Nakano, M. M. Parish, and J. Levinsen, Variational approach to the two-dimensional bose polaron, *Phys. Rev. A* **109**, 013325 (2024).

[9] S. Van Loon, W. Casteels, and J. Tempere, Ground-state properties of interacting bose polarons, *Phys. Rev. A* **98**, 063631 (2018).

[10] N. B. Jørgensen, L. Wacker, K. T. Skalmstang, M. M. Parish, J. Levinsen, R. S. Christensen, G. M. Bruun, and J. J. Arlt, Observation of attractive and repulsive polarons in a bose-einstein condensate, *Phys. Rev. Lett.* **117**, 055302 (2016).

[11] M.-G. Hu, M. J. Van de Graaff, D. Kedar, J. P. Corson, E. A. Cornell, and D. S. Jin, Bose polarons in the strongly interacting regime, *Phys. Rev. Lett.* **117**, 055301 (2016).

[12] Z. Z. Yan, Y. Ni, C. Robens, and M. W. Zwierlein, Bose polarons near quantum criticality, *Science* **368**, 190 (2020).

[13] D. Jaksch, C. Bruder, J. I. Cirac, C. W. Gardiner, and P. Zoller, Cold bosonic atoms in optical lattices, *Phys. Rev. Lett.* **81**, 3108 (1998).

[14] M. P. A. Fisher, P. B. Weichman, G. Grinstein, and D. S. Fisher, Boson localization and the superfluid-insulator transition, *Phys. Rev. B* **40**, 546 (1989).

[15] B. Capogrosso-Sansone, N. V. Prokof’ev, and B. V. Svistunov, Phase diagram and thermodynamics of the three-dimensional bose-hubbard model, *Phys. Rev. B* **75**, 134302 (2007).

[16] B. Capogrosso-Sansone, G. Söyler, N. Prokof’ev, and B. Svistunov, Monte carlo study of the two-dimensional bose-hubbard model, *Phys. Rev. A* **77**, 015602 (2008).

[17] M. Greiner, O. Mandel, T. Esslinger, T. W. Hänsch, and I. Bloch, Quantum phase transition from a superfluid to a mott insulator in a gas of ultracold atoms, *Nature* **415**, 39 (2002).

[18] W. S. Bakr, A. Peng, M. E. Tai, R. Ma, J. Simon, J. I. Gillen, S. Fölling, L. Pollet, and M. Greiner, Probing the superfluid-to-mott insulator transition at the single-atom level, *Science* **329**, 547 (2010).

[19] J. F. Sherson, C. Weitenberg, M. Endres, M. Cheneau, I. Bloch, and S. Kuhr, Single-atom-resolved fluorescence imaging of an atomic mott insulator, *Nature* **467**, 68 (2010).

[20] T. Fukuhara, A. Kantian, M. Endres, M. Cheneau, P. Schauß, S. Hild, D. Bellem, U. Schollwöck, T. Giamarchi, C. Gross, I. Bloch, and S. Kuhr, Quantum dynamics of a mobile spin impurity, *Nat. Phys.* **9**, 235 (2013).

[21] R. Alhyder, V. E. Colussi, M. Čufar, J. Brand, A. Recati, and G. M. Bruun, Lattice Bose polarons at strong coupling and quantum criticality, *SciPost Phys.* **19**, 002 (2025).

[22] M. Santiago-García, S. G. Castillo-López, and A. Camacho-Guardian, Lattice polaron in a bose-einstein condensate of hard-core bosons, *New Journal of Physics* **26**, 063015 (2024).

[23] S. Dutta and E. J. Mueller, Variational study of polarons and bipolarons in a one-dimensional bose lattice gas in both the superfluid and the mott-insulator regimes, *Phys. Rev. A* **88**, 053601 (2013).

[24] V. E. Colussi, F. Caleffi, C. Menotti, and A. Recati, Lattice polarons across the superfluid to mott insulator transition, *Phys. Rev. Lett.* **130**, 173002 (2023).

[25] K. Keiler, S. I. Mistakidis, and P. Schmelcher, Doping a lattice-trapped bosonic species with impurities: from ground state properties to correlated tunneling dynamics, *New Journal of Physics* **22**, 083003 (2020).

[26] S. Ding, G. A. Domínguez-Castro, A. Julku, A. Camacho-Guardian, and G. M. Bruun, Polarons and bipolarons in a two-dimensional square lattice, *SciPost Phys.* **14**, 143 (2023).

[27] T. Hartweg, T. Gupta, and P. Guido, The bose-hubbard polaron from weak to strong coupling, *arXiv: 2508.00486* (2025).

[28] C. Zhang, The fate of the impurity in the bose-hubbard model, (2026).

[29] N. V. Prokof'ev, B. V. Svistunov, and I. S. Tupitsyn, Worm algorithm in quantum monte carlo simulations, *JETP* **87**, 310 (1998).

[30] N. V. Prokof'ev, B. V. Svistunov, and I. S. Tupitsyn, “worm” algorithm in quantum monte carlo simulations, *Physics Letters A* **238**, 253 (1998).

[31] B. Capogrosso-Sansone, G. Söyler, N. V. Prokof'ev, and B. V. Svistunov, Critical entropies for magnetic ordering in bosonic mixtures on a lattice, *Phys. Rev. A* **81**, 053622 (2010).

[32] F. Lingua, B. Capogrosso-Sansone, A. Safavi-Naini, A. J. Jahanmiri, and V. Penna, Multiworm algorithm quantum monte carlo, *Physica Scripta* **93**, 105402 (2018).

[33] E. L. Pollock and D. M. Ceperley, Path-integral computation of superfluid densities, *Phys. Rev. B* **36**, 8343 (1987).

[34] K. V. Krutitsky, Ultracold bosons with short-range interaction in regular optical lattices, *Physics Reports* **607**, 1 (2016).

[35] C. Gross and I. Bloch, Quantum simulations with ultracold atoms in optical lattices, *Science* **357**, 995 (2017).

[36] T. Best, S. Will, U. Schneider, L. Hackermüller, D. van Oosten, I. Bloch, and D.-S. Lühmann, Role of interactions in ^{87}rb – ^{40}k bose–fermi mixtures in a 3d optical lattice, *Phys. Rev. Lett.* **102**, 030408 (2009).

[37] L. J. LeBlanc and J. H. Thywissen, Species-specific optical lattices, *Phys. Rev. A* **75**, 053612 (2007).

[38] O. Mandel, M. Greiner, A. Widera, T. Rom, T. W. Hänsch, and I. Bloch, Coherent transport of neutral atoms in spin-dependent optical lattice potentials, *Phys. Rev. Lett.* **91**, 010407 (2003).